ACS Photonics

Article

pubs.acs.org/journal/apchd5

Structural Coloring of Glass Using Dewetted Nanoparticles and Ultrathin Films of Metals

Renwen Yu,[†] Prantik Mazumder,[‡] Nick F. Borrelli,[‡] Albert Carrilero,[†] Dhriti S. Ghosh,[†] Rinu A. Maniyara,[†] David Baker,[‡] F. Javier García de Abajo,*[,†,§] and Valerio Pruneri*[,†,§]

[†]ICFO-Institut de Ciencies Fotoniques, The Barcelona Institute of Science and Technology, 08860 Castelldefels (Barcelona), Spain

[‡]Corning Inc., Sullivan Park, Corning, New York 14830, United States

[§]ICREA-Institució Catalana de Recerca i Estudis Avançats, Passeig Lluís Companys 23, 08010 Barcelona, Spain

Supporting Information

ABSTRACT: Metal nanoparticles have been used for coloring glass since antiquity. Colors are produced by light scattering and absorption associated with plasmon resonances of the particles. Recently, dewetting at high temperature has been demonstrated as a straightforward high-yield/low-cost technique for nanopatterning thin metal films into planar arrays of spherical nanocaps. Here, we show that by simply tuning the contact angle of the metal dewetted nanocaps one can achieve narrow resonances and large tunability compared with traditional approaches such as changing particle size. A vast range of colors is obtained, covering the whole visible spectrum and readily controlled by the choice of film thickness and materials. The small size of the particles results in a mild dependence on incidence illumination angle, whereas their high anisotropy gives rise to strong dichroism. We also show color tuning through interference by simply adding an ultrathin metal film at a designated distance from the dewetted particle array. Our measurements are quantitatively well explained through analytical theory, which enables fast optimization of fabrication parameters. Good agreement between theory and experiment requires incorporating the effect of plasmon peak broadening caused by the finite size distribution of the particle. The proposed designs and techniques hold great potential for large-scale production of colored and dichroic glass with application to optical windows, filters, and displays.

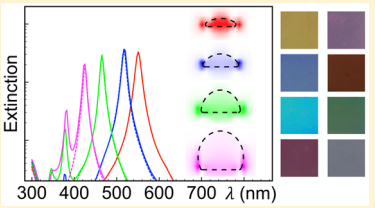

KEYWORDS: *structural colors, dewetting, plasmonics, glass coloring*

Early evidence of dichroic colored glass can be found as soon as fourth century Rome: the celebrated Lycurgus Cup,[1] whose color changes between red and green depending on the illumination angle. We had to wait until recent times to understand that coloring was produced by dispersed silver nanoparticles, whose localized surface plasmon resonances (LSPRs) affect very differently the light spectra in either reflection or transmission. Based on this effect and on the dependence of LSPRs on particle size, shape, and composition, various strategies have been explored for structural coloring,[2−12] including LSPR hybridization in metal nanodisks and nanoholes.[13]

Modern dichroic colored glass is however based on thin-film interference, which is widely used in a variety of commercial optical filters[14] to produce narrow spectral bands for applications such as fluorescence microscopy[15] and LCD projectors.[16] On the exploratory side, intense research efforts are being devoted to creating bright structural colors through thin-film interference involving ultrathin metal films (UTMFs)[17] and lossy dielectric layers on top of metals.[18]

In many applications it is crucial to create colors in a transparent substrate (e.g., glass) via surface nanostructuring.[19] This is a flexible strategy that can be applied to virtually any glass and does not require bulk modifications, such as the addition of inclusions. However, in order to attract industrial interest, it must be low cost and mass scalable. Intensive optical and electron-beam nanolithography are therefore not an option. Instead, dewetting of UTMFs has recently been shown to provide an efficient way of forming metal nanoparticles on large silica surfaces.[20−22] The process consists in depositing a continuous UTMF and heating it to several hundred degrees Celcius, so that the film contiguity disappears and the metal groups together into nanoparticles with characteristic size distributions. Surface energies of UTMF and substrate as well as the interfacial energy between them drive the particle shape into nanocaps of well-determined contact angle β with the substrate.[23] Interestingly, the particle size and surface density can be controlled by the original film thickness, as well as by the duration and temperature of the heating treatment.[24] Metal dewetting is thus a viable option for simple, low-cost lithography-free surface nanostructuring, which is ideal for industrially scalable applications.

Here, we demonstrate the use of dewetted metal nanocaps on transparent silica surfaces to produce and customize structural colors. In particular, we demonstrate for the first time that by changing the contact angle of the nanocaps we can obtain larger tuning and narrower LSPRs than traditional

Received: February 10, 2016

DOI: 10.1021/acsphotonics.6b00090
ACS Photonics XXXX, XXX, XXX−XXX

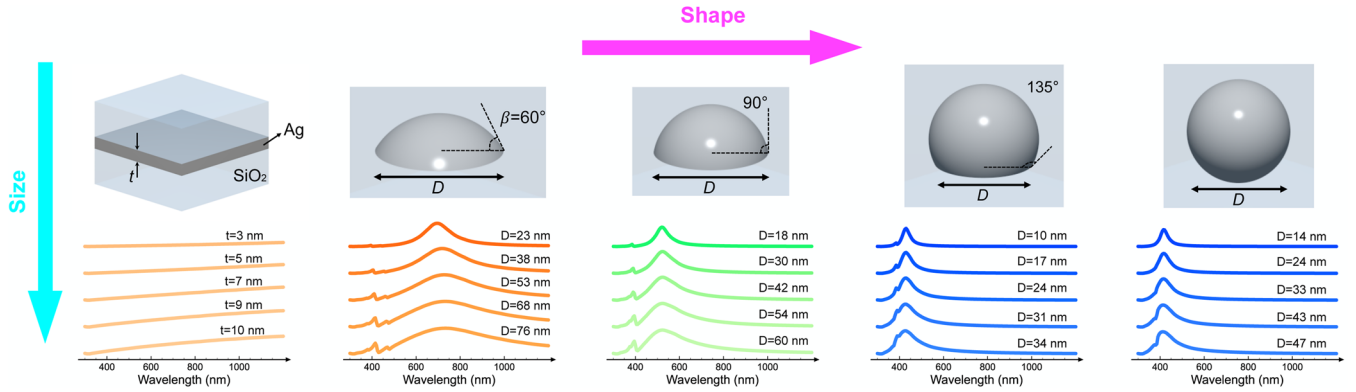

Figure 1. Color tuning through particle size and shape. Top: Geometry and parameters of a silver ultrathin metal film (UTMF) of thickness t, along with nanocaps of various shapes and sizes (base diameter D and contact angle β), produced upon dewetting of the film. The metal is embedded in silica. We assume the nanocaps to be distributed in a triangular lattice with spacing $8t$ and total metal volume equal to that of the homogeneous UTMF in all cases. Bottom: Calculated normal-incidence reflection spectra for particles of varying shape (horizontal direction) and size (vertical). Each curve is given the RGB color extracted from the spectrum that it represents.

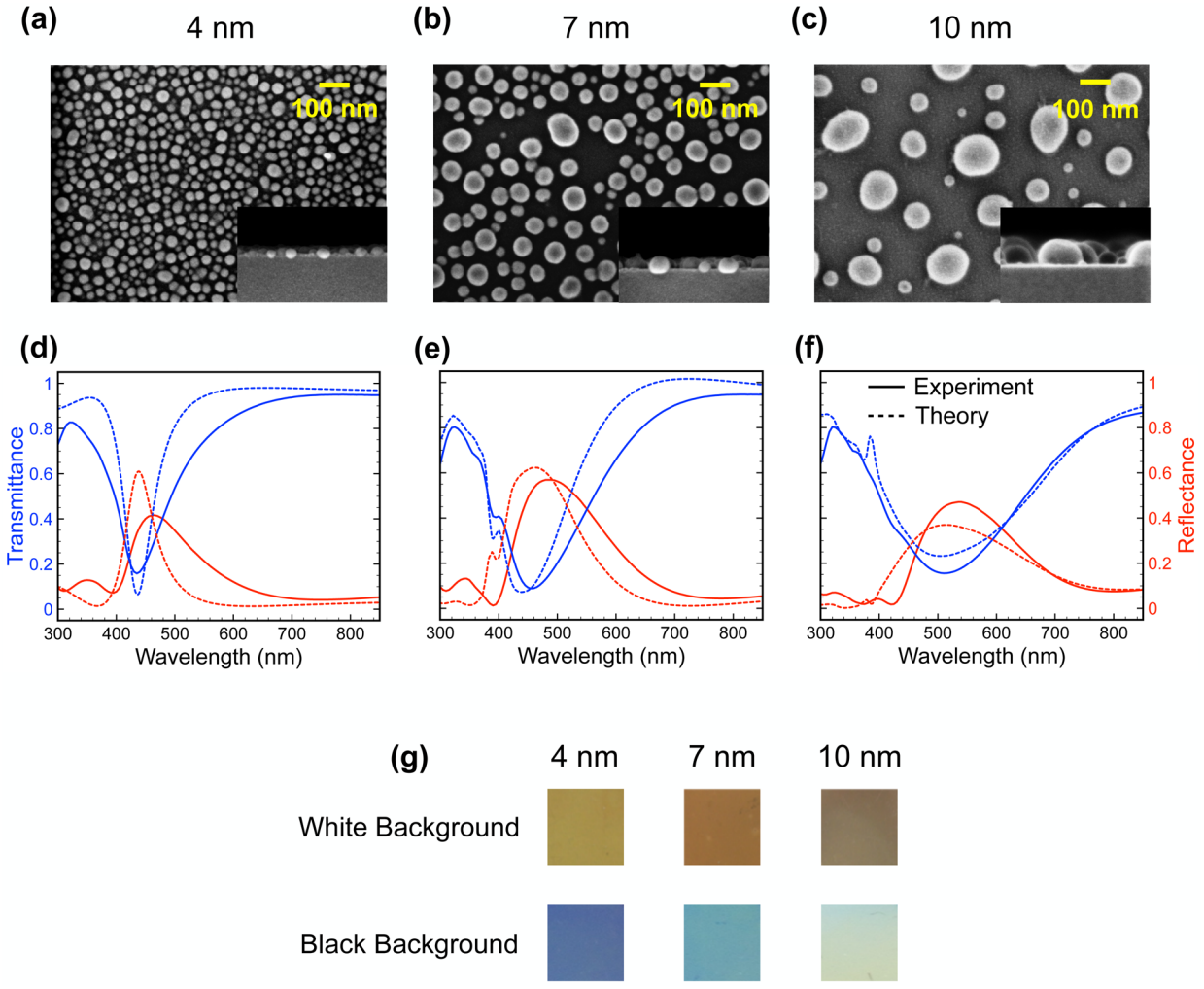

Figure 2. Color tuning through UTMF dewetting. We illustrate this concept with three representative samples produced upon dewetting of silver UTMFs. (a–c) Sample SEM images for different initial silver UTMF thicknesses (i.e., before dewetting; see top labels and also Table 1). (d–f) Measured (solid curves) and calculated (broken curves) normal-incidence transmission (blue curves) and reflection (red curves) spectra for the samples shown in (a)–(c). (g) Photographs for the three samples with measured spectra corresponding to (d)–(f) on white and black backgrounds.

approaches, for example, relying on changing particle size. A wide chromatic range is also accessible through varying the initial film thickness. The structures display a high degree of dichroism, with radically different colors on transmission and reflection. We mainly focus on silver-on-silica, for which the contact angle determines the nanocap morphology, although

DOI: 10.1021/acsphotonics.6b00090
ACS Photonics XXXX, XXX, XXX–XXX

the method can be generally applied to other combinations of metal film and dielectric substrate. We gain further flexibility in color range and spectral absorbance by creating interfering structures with the addition of another properly spaced UTMF.

RESULTS AND DISCUSSION

The power of changing the contact angle of nanocaps and of a straightforward dewetting process for structural coloring is clearly illustrated by Figure 1, which shows simulated reflection spectra of uniform and dewetted silver UTMFs embedded in silica for typical geometrical parameters similar to those of the actual samples (see below). When the UTMF thickness is increased in the t = 3−10 nm range, the reflectance gradually grows at long wavelengths. This effect has a minor influence on reflection structural colors, which are mostly faded red (see Figure 1, in which different curves are given the RGB color computed from the spectra that they represent; see Materials and Methods for more details). However, a radical change in color is observed when moving from continuous UTMFs to dewetted nanocaps with different sizes and shapes (contact angle). As we show below, the average base diameter D and contact angle β can be controlled by the dewetting temperature, the duration of the thermal treatment used to induce dewetting, and the initial UTMF thickness; so these parameters allow us to generate on-demand bright structural colors, which are in all cases associated with the excitation of LSPRs in the nanocaps. In particular, we observe an excursion along a red-green-blue hue when the contact angle is varied in the β = 60−135° range, driven by a change in plasmon resonance position. Generally, colors become lighter as the nanocap base diameter increases, due to LSPR broadening produced by radiative losses of the individual particles. For illustration, all reflection spectra of Figure 1 are calculated for triangular lattices of spacing 8t, with nanocap size determined by the condition that the metal volume is maintained as in the initial film of thickness t, which results in the values of the base diameter D indicated by labels. Reflection spectra for spheres are also provided as a reference. Incidentally, we observe similar trends when examining arrays of particles with fixed base diameter but varying contact angle, in which the spacing is adjusted in order to maintain total metal volume as a constant (see Figure S1 in the Supporting Information (SI) for calculations of the transmittance as a function of light wavelength and incidence angle, indicating that LSPR-based coloring is robust against changes of incidence angle). In contrast to previous work, which focused on changing particle size (diameter), our proposed tuning scheme, relying on changing the contact angle, is much wider. Additionally, previous work has also shown that periodic structures can be used to achieve structural coloring, tuning the plasmonic response by changing the period.[32−34] However, such approaches suffer from either broad resonance features[32,33] or strong angular dependence of the obtained color.[34]

We corroborate the potential of UTMF dewetting for coloring by preparing and optically characterizing samples consisting of silver on silica with different metal thicknesses (see Materials and Methods for fabrication details). A nearly index-matching 150 nm thick layer of poly(methyl methacrylate) (PMMA) is deposited on top (2% difference with the refractive index of the silica substrate; similar results are obtained with silica embedding; see Figure S2 in the SI). The results are summarized in Figure 2. In particular, Figure 2a−c shows SEM images of three samples, which produce the transmission and reflection spectra plotted in Figure 2d−f, and these in turn generate the colors shown in Figure 2g.

As a rule, a larger initial metal thickness gives rise to lower particle density and larger particle size (Figure 2a−c). This increase in size switches on retardation, which in turn produces plasmon broadenings and red-shifts (Figure 2d−f). Similar conclusions can be extracted from samples of nanocaps exposed to air (see Figure S2 in the SI), but now the LSPRs are blue-shifted with respect to those covered with PMMA. The dielectric protection also prevents silver oxidation: we have verified their stable optical properties over a period of several months.

Figure 2g displays photographs taken from these three samples (Figure 2d−f). A large contrast in structural colors depending on whether the samples are on white or black background is evident.

We seek further understanding of our measurements (Figure 2d−f, solid curves) by formulating an analytical theoretical model (broken curves), which is in excellent agreement with experiment in the details of the reflection/transmission spectra (Figure 2d−f). The model uses as input the geometrical parameters retrieved upon inspection of the sample SEM images (Figure 2a−c), which are summarized in Table 1. We

Table 1. Statistical Parameters for Three Fabricated Samples with Different Initial Silver UTMF Thicknesses, as Extracted by SEM Image Analysis[a]

initial film thickness (nm)	particle density (μm^{-2})	average base diameter (nm)	diameter std (nm)	average height (nm)	estimated contact angle (deg)
4	805	20	9	16	116
7	210	34	14	35	128
10	35	82	30	71	120

[a]See Figure 2a−c. The contact angle is estimated from the height and base diameter assuming spherical nanocap profiles.

describe the particles as spherical nanocaps similar to those of Figure 1 and assume a fixed value of the silver-on-silica contact angle β = 120°. The optical response of the nanocaps is reduced to their average anisotropic polarizability (for axial and transversal directions), which we combine with the dynamical interaction between them, taking into account their random distribution, to produce reflection and transmission coefficients (see Materials and Methods for more details). This model produces satisfactory results compared with experiment (Figure 2d−f), except for the discrepancy in plasmon width of the thinner sample (Figure 2d), where the particle details are at the limit of the SEM spatial resolution, which probably affects the determination of statistic geometrical parameters.

The optical response of our samples emerges from the properties of the individual nanocaps and their LSPRs, which we investigate in more detail in Figure 3. In particular, the dependence on contact angle β is summarized in Figure 3a−c for small nanocaps (base diameter D = 10 nm), for which retardation can be neglected. The response in the spectral range under consideration is dominated by the lowest order axial and transversal dipolar plasmons, whose spectral position and weight are fully captured by two parameters in the electrostatic limit, which we extract from boundary-element method electromagnetic simulations[25] (BEM; see methods): the value of the metal permittivity at which the plasmon shows up (Figure 3a) and the dipolar transition strength (Figure 3b). The

DOI: 10.1021/acsphotonics.6b00090
ACS Photonics XXXX, XXX, XXX−XXX

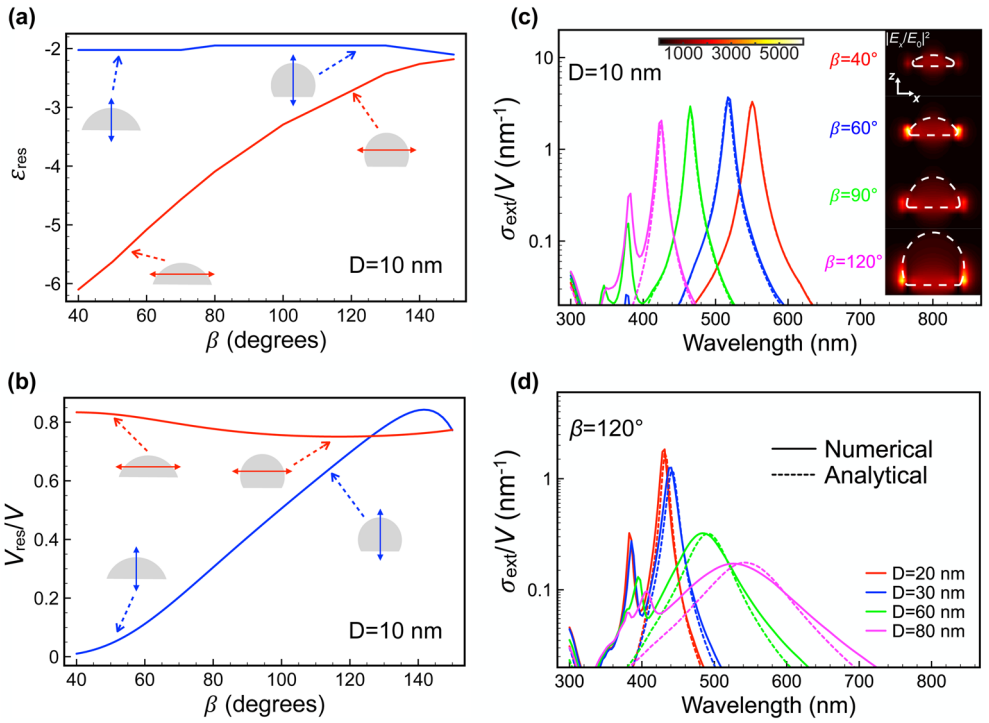

Figure 3. Plasmons in spherical nanocaps. (a) Resonant value of the permittivity for which a dipolar plasmon is sustained by nanocaps of varying shape (i.e., as a function of contact angle β). Both transversal and axial polarizations are considered (see insets and double arrows). (b) Fractional contribution to the spectral weight for the plasmons considered in (a). (c) Normalized extinction spectra of these nanocaps for light incident along the axial direction. Numerical electromagnetic simulations (solid curves) are well reproduced by a simple analytical model (dashed curves; see Materials and Methods) based on the dominant transversal plasmon. (d) Same as (c) for nanocaps of fixed shape (β = 120°) and different larger sizes (the legend indicates the base diameter legend D), illustrating the ability of our model to cope with retardation effects (see Materials and Methods).

latter is expressed in terms of a fractional volume associated with the resonance, and it amounts to the fraction that it contributes to the integral of the extinction cross-section over frequency. These two parameters are all the input that we need to analytically describe the polarizability of the particles (see Materials and Methods), from which we calculate the cross-section represented in Figure 3c (broken curves). Despite the simplicity of this method, we find a remarkable agreement of the spectra with BEM simulations (broken curves). Notice that under light incidence along the particle axis the transversal plasmon dominates the response. Near-field plots associated with this mode reveal light confinement and enhancement near the edge of the particle base (see insets to Figure 3c). Unlike the axial plasmon, the transversal one has a strong dependence on contact angle (Figure 3a), whereas its spectral weight remains at a high level of ~0.8 (Figure 3b). This explains the weak dependence of the optical properties of our samples on incidence angle. Nevertheless, the axial plasmon can also be excited in our nanostructures at larger incidence angle, emerging as a feature at shorter wavelength (see Figure S1 in the SI).

When the particle size increases, retardation effects become important, leading to plasmon red-shifting and broadening. Both of these effects can be easily accounted for in a modified analytical polarizability that we present in Materials and Methods. The results are in excellent agreement with electromagnetic BEM simulations, as illustrated in Figure 3d for nanocaps of shape and sizes similar to those involved in the measured samples of Figure 2. Additionally, the dominant plasmon feature in the spectra is expected to blue-shift with increasing contact angle (see Figure 3c), as the particle aspect ratio is reduced. This result is fully corroborated by measurements on additional samples in which a treatment of the surface can produce a change in contact angle (see Figure S3 in the SI). Further comparisons between numerical and theoretical results for nanocaps with other contact angles are offered in Figure S4 of the SI.

Optical interference can also produce structural colors, adding an extra knob to further tune the chromatic suite achieved through metal dewetting. We test this principle by adding an extra nickel layer of thickness varied from d = 3 nm (transparent) to 40 nm (opaque). In particular, we show in Figure 4a results for samples produced by this procedure f4 starting with a dewetted 7 nm silver film, covered with 150 nm of PMMA. A clear asymmetric plasmonic coloring effect is observed in measurements from the two sides of the sample (*front* and *back*, see scheme in Figure 4a). Transmittance from both sides is identical in virtue of reciprocity, as corroborated in both measurements and simulations (see Figure 4b and also Figure S5 in the SI), and it eventually evolves toward negligible values as the nickel eventually becomes optically thick. In contrast, there are clear differences in absorbance from both sides: front-side absorption increases with nickel thickness d in the 300−550 nm wavelength range, reaching values above 85%, essentially as a result of a Salisbury screen effect;[35] however, back-side absorption decreases with increasing d, attenuating the effect of the dewetted silver layer and eventually saturating at the bulk nickel surface absorption level. The chromatic variation produced upon nickel deposition is illustrated by photographs in Figure 4c. We note that both in the spectra and

DOI: 10.1021/acsphotonics.6b00090
ACS Photonics XXXX, XXX, XXX−XXX

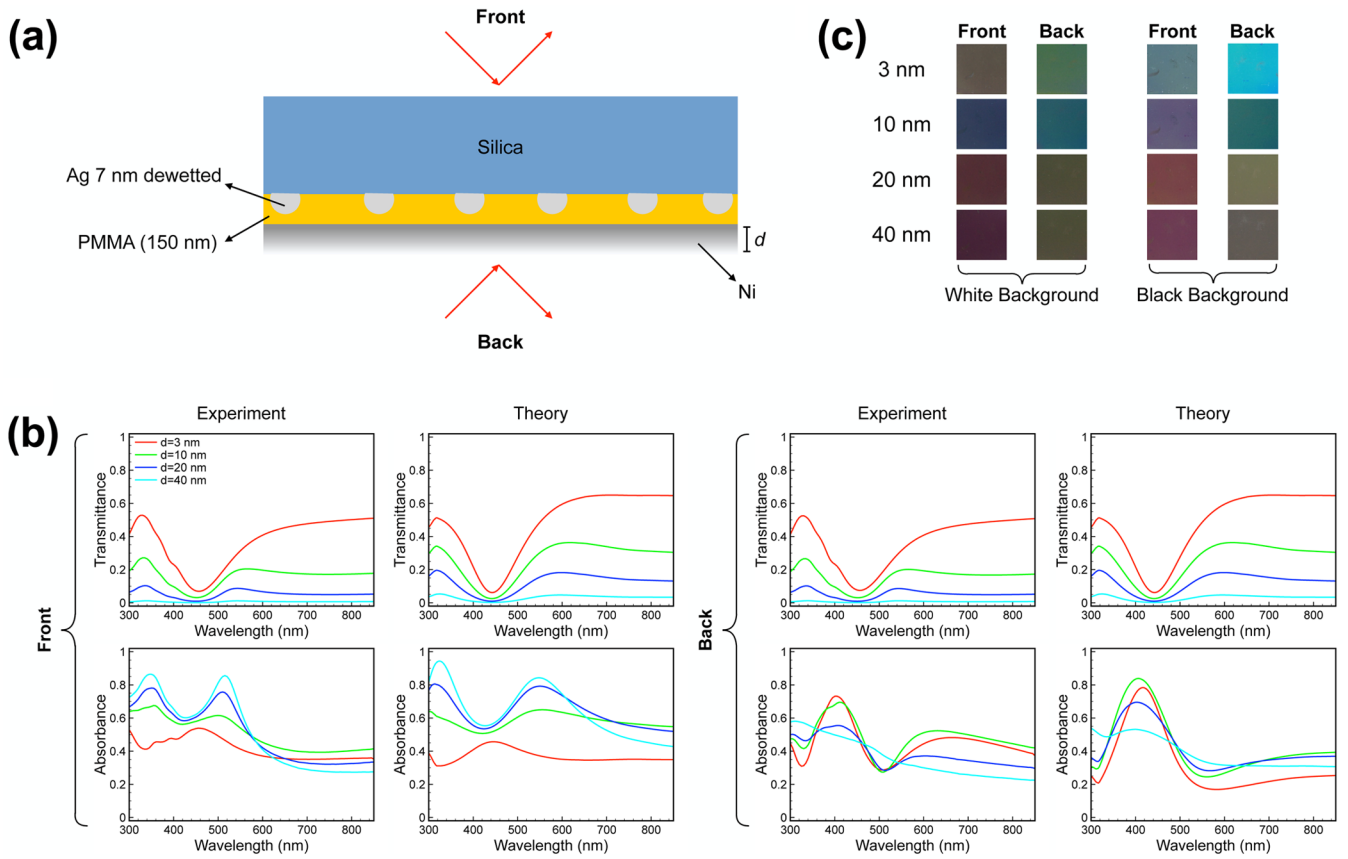

Figure 4. Additional color tuning through interference. (a) A nickel UTMF is deposited on a 150 nm PMMA spacer embedding the silver nanocaps that are previously obtained upon dewetting a 7 nm silver film. (b) Measured and calculated transmission and absorption spectra for normal-incidence illumination from the back and front sides of the structure (see (a)). We consider different nickel thicknesses in the d = 3−40 nm range. (c) Photographs of the samples whose measured absorption (reflection) spectra are shown in (b), taken on white and black backgrounds.

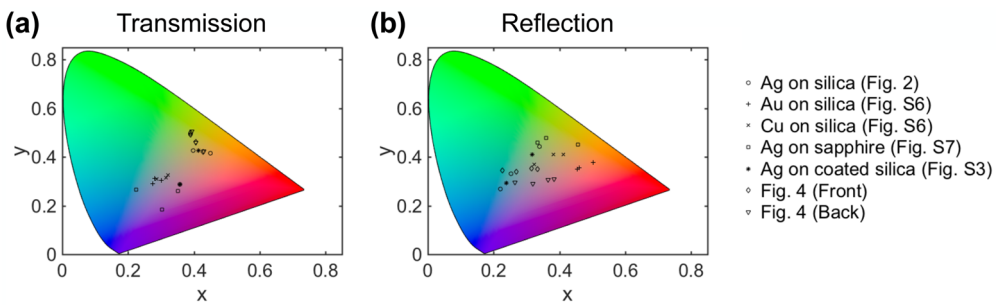

Figure 5. Position of the colors in our samples on the CIE 1931 map. We show the colors associated with our experimental spectra (see labels), as obtained for a D65 illumination light source.

in the resulting colors our simple theory compares reasonably well with experiment, including in this case the effect of multiple reflections at the different interfaces of the sample.

CONCLUSION

In summary, we have demonstrated that arrays of metal nanocaps created via a low-cost, lithography-free dewetting process display intense colors as a result of the excitation of localized surface plasmons in the particles. A wide chromatic range is accessible through careful control of the initial metal thickness and the dewetting conditions (temperature and duration), which ultimately defines the size, density, and contact angle of the resulting nanoparticles. Colors can be actually customized over a sizable range of the visible spectrum for a wide range of incidence angles, as shown in Figure 5, where we represent the colors associated with our obtained experimental spectra superimposed on the Commission Internationale de l'Elcairage (CIE) 1931 color map. For example, we observe structures that go from reflective (scattered) red to green and blue, suggesting the potential for large-scale manufacturing of structurally colored glass windows, optical filters, and display panels.[36] The addition of an extra ultrathin metal film produces interference with the dewetted film, leading to further control over the chromatic properties. The combination of continuous and dewetted metal layers thus holds great potential to achieve full control over the visible spectral properties of thin films, which are accessible though industrially scalable, economic fabrication processes. Our

DOI: 10.1021/acsphotonics.6b00090
ACS Photonics XXXX, XXX, XXX−XXX

results can be readily extrapolated to other spectral regimes through a choice of appropriate materials (e.g., aluminum for the UV).

MATERIALS AND METHODS

Ultrathin Metal Film Deposition and Dewetting. Silver ultrathin films are deposited on the silica substrate using a magnetron sputtering system (ATC Orion 8, AJA International, Inc. or KDF 903i). The coated substrates are then subjected to rapid thermal annealing in a Tsunami RTP-600S at a temperature of 750 °C for about 90 s under a nitrogen flow of 1 atm. In this way the ultrathin silver films are dewetted into nanocaps. The PMMA overlayer is deposited through spin-coating.

Sample Characterization. Optical transmittance and reflectance are measured using a UV−vis−NIR spectrophotometer (PerkinElmer Lambda 950). The morphology of the nanocaps is examined with a field-emission scanning electron microscope (FEG-SEM, Inspect F, FEI Systems).

Simulation of Individual Nanocaps. The optical response of individual nanocaps is simulated using BEM.[25] The metal dielectric function is taken from tabulated data,[26] whereas a homogeneous surrounding medium is assumed with constant permittivity $\epsilon_s = 2.13$ similar to that of silica and PMMA in the spectral region under investigation. The particle geometry is determined by its base diameter D and contact angle with the substrate β, while the edges are smoothed with a rounded radius of 0.5 nm. These simulations yield the particle extinction cross-section and its scattering matrix used to simulate arrays.

Average Polarizability of Nanocaps in the Actual Samples. For a given sample, the contact angle is roughly constant, and in particular, it takes the value $\beta = 120°$ for silver on silica. However, the particle size has a finite size distribution, which we describe through a Gaussian,

$$P(D) = \frac{1}{\sqrt{2\pi}\,\sigma} e^{-(D-\bar{D})^2/2\sigma^2}$$

as a function of the base diameter D, centered around its average $\bar{D}$ with standard deviation σ. These parameters ($\bar{D}$ and σ) depend on the initial UTMF thickness, as shown in Table 1. We then describe the particles through their average polarizability:

$$\bar{\alpha}_{\parallel,\perp}(\omega) = -\frac{1}{k^2}\int f_{\parallel,\perp}(\omega, D)\, P(D)\, \mathrm{d}D$$

where $f_{\parallel,\perp}(\omega,D)$ is the far-field amplitude of individual nanocaps for transversal ($\perp$) and axial ($\parallel$) incident field polarization, calculated with BEM as noted above.

Analytical Model for Individual Nanocaps. We elaborate an analytical model based upon the dipolar response of the particles, supplemented to incorporate retardation effects, which are important for large sizes, although the particle diameters under consideration are still small compared with the wavelength, so that the dipolar response becomes dominant. In the electrostatic limit, the particle polarizability can be written as[27]

$$\alpha_{es}(\omega) = \frac{1}{4\pi\epsilon_s}\sum_j V_j\left[\frac{1}{\epsilon(\omega)-\epsilon_s} - \frac{1}{\epsilon_s(\epsilon_j - 1)}\right]^{-1}$$

where $\epsilon(\omega)$ and ϵ_s are the permittivities of the metal in the particle and the dielectric host, respectively. Here, the sum extends over the electrostatic eigenmodes of the system, which are identified by eigenvalues ϵ_j and contribute to the polarizability with a partial volume V_j (the sum of V_j's is equal to the particle volume). Retardation produces two effects: (1) radiative damping, which we incorporate through the well-known prescription[28]

$$\alpha(\omega) = \frac{1}{\alpha_{es}^{-1} - 2ik^3/3}$$

where $k = \omega/c$; and (2) plasmon red-shifts, which we phenomenologically describe through the substitution

$$\epsilon_j \to \frac{\epsilon_j}{\cos(k\xi D)} + \left[1 - \frac{1}{\cos(k\xi D)}\right]\frac{1}{\epsilon_s}$$

where ξ is a scaling factor. Finally, we compare the extinction cross-section computed with BEM (see above) with the analytical cross-section $4\pi k\mathrm{Im}\{\alpha(\omega)\}$ in order to extract fitting parameters ϵ_j, V_j, and ξ, which depend only on the geometrical contact angle β, but not on material composition and frequency. In particular, we find $\xi = 0.75$ for the contact angle $\beta = 120°$ of silver on silica. In practice, we retain only the lowest order dipolar mode for polarization directions either parallel to the nanocap base (transverse) or along its rotation axis (axial).

Simulation of Periodic Nanocap Arrays. We use the layer-KKR method[29] to simulate the response of periodic particle arrays (see Figure S1 in the SI). A rigorous solution of Maxwell's equations is then obtained by describing the particles through their scattering matrix (i.e., their multipolar response), as obtained with BEM (see above).

Analytical Model for Disordered Nanocap Arrays. We formulate an analytical model of the response of the samples by describing the nanocaps through the average polarizability $\bar{\alpha}$ (see above), following similar methods to those reported elsewhere.[30,31] In particular, the reflection and transmission coefficients for p-polarized light with angle of incidence θ reduce to

$$r = \frac{i2\pi k\rho}{\cos\theta}\left(\frac{-\cos^2\theta}{\bar{\alpha}_{\parallel}^{-1} - G_{\parallel}} + \frac{\sin^2\theta}{\bar{\alpha}_{\perp}^{-1} - G_{\perp}}\right)$$

$$t = 1 - r + \frac{i2\pi k\rho}{\cos\theta}\frac{2\sin^2\theta}{\bar{\alpha}_{\perp}^{-1} - G_{\perp}}$$

where ρ is the particle density, whereas $G_{\parallel,\perp}$ are the dipole−dipole interaction lattice sums. The latter allows the expression

$$G_{\parallel,\perp} = \int \frac{d^2\mathbf{Q}}{(2\pi)^2}\left[\frac{1}{\rho}S(\mathbf{Q}-\mathbf{k}_{\parallel}) - 1\right]\mathcal{G}_{\parallel,\perp}(\mathbf{Q})$$

in terms of the momentum representation of the dipole−dipole interaction components $\mathcal{G}_{\perp}(\mathbf{Q}) = 2\pi i k_z Q_x^2/Q^2 + 2\pi i(k^2/k_z)(1 - Q_x^2/Q^2)$ and $\mathcal{G}_{\parallel}(\mathbf{Q}) = 2\pi i Q^2/k_z$, where $k_z = \sqrt{k^2 - Q^2}$, as extracted for both interacting dipoles oriented either perpendicular or parallel to the surface normal, respectively. The lattice sums also depend on the surface projection of the incident light wave vector $\mathbf{k}_{\parallel}$ and the structure factor $S(\mathbf{Q}) = \sum_{\mathbf{R}} \exp(i\mathbf{Q}\cdot\mathbf{R})$, where the sum runs over particle positions. More precisely, we have

DOI: 10.1021/acsphotonics.6b00090
ACS Photonics XXXX, XXX, XXX−XXX

$S(\mathbf{Q}) = (2\pi\rho)^2\delta(\mathbf{Q}) + \rho$ for a completely disordered array and $S(\mathbf{Q}) = (2\pi\rho)^2\sum_{\mathbf{g}} \delta(\mathbf{Q}-\mathbf{g})$ for a periodic one, where $\mathbf{g}$ runs over reciprocal lattice vectors. Theory curves in Figures 2 and 4 are obtained assuming random particle distributions.

RGB Color. We show RGB colors in several figures, as extracted from measured and calculated spectra, assuming a flat-spectrum illumination. RGB parameters are obtained simply by projection on the spectra of the three pigments that define this color scheme.

■ ASSOCIATED CONTENT

Supporting Information

The Supporting Information is available free of charge on the ACS Publications website at DOI: 10.1021/acsphotonics.6b00090.

Further simulations and experiments and, in particular, calculations of the transmittance of ordered and disordered planar particle arrays for fixed particle size and different contact angles (Figure S1); measured reflection and transmission spectra for silver nanocaps with different surrounding media (Figure S2) and contact angles (Figure S3 and Table S1); an extension of Figure 3d to cover more contact angles (Figure S4); the reflectance spectra corresponding to the samples of Figure 4b (Figure S5); and measured spectra for gold and copper on silica (Figure S6) and silver on sapphire (Figure S7) (PDF)

■ AUTHOR INFORMATION

Corresponding Authors

*E-mail: javier.garciadeabajo@icfo.es.

*E-mail: valerio.pruneri@icfo.es.

Notes

The authors declare no competing financial interest.

■ ACKNOWLEDGMENTS

This work has been supported in part by Spanish MINECO (MAT2014-59096-P and SEV2015-0522), Fundació Privada Cellex, the European Commission (Graphene Flagship CNECT-ICT-604391 and FP7-ICT-2013-613024-GRASP), AGAUR (2014 SGR 1400 and 1623), and the Fondo Europeo de Desarrollo Regional (FEDER, TEC2013-46168-R).

■ REFERENCES

(1) Freestone, I.; Meeks, N.; Sax, M.; Higgitt, C. The Lycurgus Cup - A Roman nanotechnology. *Gold Bulletin* **2007**, *40*, 270−277.

(2) Kinoshita, S.; Yoshioka, S.; Miyazaki, J. Physics of structural colors. *Rep. Prog. Phys.* **2008**, *71*, 076401.

(3) Inoue, D.; Miura, A.; Nomura, T.; Fujikawa, H.; Sato, K.; Ikeda, N.; Tsuya, D.; Sugimoto, Y.; Koide, Y. Polarization independent visible color filter comprising an aluminum film with surface-plasmon enhanced transmission through a subwavelength array of holes. *Appl. Phys. Lett.* **2011**, *98*, 093113.

(4) Lee, H.-S.; Yoon, Y.-T.; Lee, S.-s.; Kim, S.-H.; Lee, K.-D. Color filter based on a subwavelength patterned metal grating. *Opt. Express* **2007**, *15*, 15457−15463.

(5) Roberts, A. S.; Pors, A.; Albrektsen, O.; Bozhevolnyi, S. I. Subwavelength plasmonic color printing protected for ambient use. *Nano Lett.* **2014**, *14*, 783−787.

(6) Si, G.; Zhao, Y.; Lv, J.; Lu, M.; Wang, F.; Liu, H.; Xiang, N.; Huang, T. J.; Danner, A. J.; Teng, J.; Liu, Y. J. Reflective plasmonic color filters based on lithographically patterned silver nanorod arrays. *Nanoscale* **2013**, *5*, 6243−6248.

(7) Xu, T.; Wu, Y.-K.; Luo, X.; Guo, L. J. Plasmonic nanoresonators for high-resolution colour filtering and spectral imaging. *Nat. Commun.* **2010**, *1*, 59.

(8) Kumar, K.; Duan, H.; Hegde, R. S.; Koh, S. C. W.; Wei, J. N.; Yang, J. K. W. Printing colour at the optical diffraction limit. *Nat. Nanotechnol.* **2012**, *7*, 557−561.

(9) Cheng, F.; Gao, J.; Luk, T. S.; Yang, X. Structural color printing based on plasmonic metasurfaces of perfect light absorption. *Sci. Rep.* **2015**, *5*, 11045.

(10) Li, Z.; Clark, A. W.; Cooper, J. M. Dual Color Plasmonic Pixels Create a Polarization Controlled Nano Color Palette. *ACS Nano* **2016**, *10*, 492−498.

(11) Clark, A. W.; Cooper, J. M. Plasmon Shaping by using Protein Nanoarrays and Molecular Lithography to Engineer Structural Color. *Angew. Chem.* **2012**, *124*, 3622−3626.

(12) Olson, J.; Manjavacas, A.; Liu, L.; Chang, W.-S.; Foerster, B.; King, N. S.; Knight, M. W.; Nordlander, P.; Halas, N. J.; Link, S. Vivid, full-color aluminum plasmonic pixels. *Proc. Natl. Acad. Sci. U. S. A.* **2014**, *111*, 14348−14353.

(13) Clausen, J. S.; Højlund-Nielsen, E.; Christiansen, A. B.; Yazdi, S.; Grajower, M.; Taha, H.; Levy, U.; Kristensen, A.; Mortensen, N. A. Plasmonic metasurfaces for coloration of plastic consumer products. *Nano Lett.* **2014**, *14*, 4499−4504.

(14) Macleod, H. A. *Thin-Film Optical Filters*; CRC Press, 2001.

(15) Lichtman, J. W.; Conchello, J. A. Fluorescence microscopy. *Nat. Methods* **2005**, *2*, 910−919.

(16) Sampsell, J. B.; Florence, J. M. Projection display system for reflective light valves. U.S. Patent US6,113,239, 2000.

(17) Li, Z.; Butun, S.; Aydin, K. Large-Area, Lithography-Free Super Absorbers and Color Filters at Visible Frequencies Using Ultrathin Metallic Films. *ACS Photonics* **2015**, *2*, 183−188.

(18) Kats, M. A.; Blanchard, R.; Genevet, P.; Capasso, F. Nanometre optical coatings based on strong interference effects in highly absorbing media. *Nat. Mater.* **2013**, *12*, 20−24.

(19) Nassau, K. *The Physics and Chemistry of Color: The Fifteen Causes of Color*; Wiley-VCH: New York, 2001.

(20) Yan, M.; Dai, J.; Qiu, M. Lithography-free broadband visible light absorber based on a mono-layer of gold nanoparticles. *J. Opt.* **2014**, *16*, 025002.

(21) Mazumder, P.; Jiang, Y.; Baker, D.; Carrilero, A.; Tulli, D.; Infante, D.; Hunt, A. T.; Pruneri, V. Superomniphobic, transparent, and antireflection surfaces based on hierarchical nanostructures. *Nano Lett.* **2014**, *14*, 4677−4681.

(22) Tulli, D.; Hart, S. D.; Mazumder, P.; Carrilero, A.; Tian, L.; Koch, K. W.; Yongsunthon, R.; Piech, G. A.; Pruneri, V. Monolithically Integrated Micro- and Nanostructured Glass Surface with Antiglare, Antireflection, and Superhydrophobic Properties. *ACS Appl. Mater. Interfaces* **2014**, *14*, 11198−11203.

(23) Thompson, C. V. Solid-state dewetting of thin films. *Annu. Rev. Mater. Res.* **2012**, *42*, 399−434.

(24) Infante, D.; Koch, K. W.; Mazumder, P.; Tian, L.; Carrilero, A.; Tulli, D.; Baker, D.; Pruneri, V. Durable, superhydrophobic, antireflection, and low haze glass surfaces using scalable metal dewetting nanostructuring. *Nano Res.* **2013**, *6*, 429−440.

(25) García de Abajo, F. J.; Howie, A. Retarded field calculation of electron energy loss in inhomogeneous dielectrics. *Phys. Rev. B: Condens. Matter Mater. Phys.* **2002**, *65*, 115418.

(26) Johnson, P. B.; Christy, R. W. Optical constants of the noble metals. *Phys. Rev. B* **1972**, *6*, 4370−4379.

(27) Solís, D. M.; Taboada, J. M.; Obelleiro, F.; Liz-Marzán, L. M.; García de Abajo, F. J. Toward ultimate nanoplasmonics modeling. *ACS Nano* **2014**, *8*, 7559−7570.

(28) Draine, B. T. The discrete-dipole approximation and its application to interstellar graphite grains. *Astrophys. J.* **1988**, *333*, 848−872.

(29) Stefanou, N.; Yannopapas, V.; Modinos, A. MULTEM 2: A new version of the program for transmission and band-structure calculations of photonic crystals. *Comput. Phys. Commun.* **2000**, *132*, 189−196.

DOI: 10.1021/acsphotonics.6b00090
ACS Photonics XXXX, XXX, XXX−XXX

(30) García de Abajo, F. J. Colloquium: Light scattering by particle and hole arrays. *Rev. Mod. Phys.* **2007**, *79*, 1267−1290.
(31) Stauber, G. G.; García de Abajo, F. J. Extraordinary absorption of decorated undoped graphene. *Phys. Rev. Lett.* **2014**, *112*, 077401.
(32) Shrestha, V. R.; Lee, S.-S.; Kim, E.-S.; Choi, D.-Y. Aluminum plasmonics based highly transmissive polarization-independent subtractive color filters exploiting a nanopatch array. *Nano Lett.* **2014**, *14*, 6672−6678.
(33) Tan, S. J.; Zhang, L.; Zhu, D.; Goh, X. M.; Wang, Y. M.; Kumar, K.; Qiu, C.-W.; Yang, J. K. Plasmonic color palettes for photorealistic printing with aluminum nanostructures. *Nano Lett.* **2014**, *14*, 4023−4029.
(34) Shen, Y.; Rinnerbauer, V.; Wang, I.; Stelmakh, V.; Joannopoulos, J. D.; Soljacic, M. Structural colors from Fano resonances. *ACS Photonics* **2015**, *2*, 27−32.
(35) Munk, B. A. *Frequency Selective Surfaces: Theory and Design*; John Wiley & Sons, 2005.
(36) Hsu, C. W.; Zhen, B.; Qiu, W.; Shapira, O.; DeLacy, B. G.; Joannopoulos, J. D.; Soljačić, M. Transparent displays enabled by resonant nanoparticle scattering. *Nat. Commun.* **2014**, *5*, 3152.

DOI: 10.1021/acsphotonics.6b00090
ACS Photonics XXXX, XXX, XXX−XXX